Microelectromechanical-System-Based Design of a High-Finesse Fiber Cavity Integrated with an Ion Trap

Moonjoo Lee,[1,‡] Minjae Lee,[2,‡] Seokjun Hong,[2] Klemens Schüppert,[1] Yeong-Dae Kwon,[3] Taehyun Kim,[4] Yves Colombe,[1] Tracy E. Northup,[1,*] Dong-Il "Dan" Cho,[2,†] and Rainer Blatt[1,5]

[1] *Institut für Experimentalphysik, University of Innsbruck, Technikerstraße 25, 6020 Innsbruck, Austria*

[2] *ISRC/ASRI, Department of Electrical and Computer Engineering, Seoul National University, Seoul 151-744, Republic of Korea*

[3] *Quantum Technology Laboratory, SK Telecom, Seongnam-si 463-784, Republic of Korea*

[4] *ICT/ASRI, Department of Computer Science and Engineering, Seoul National University, Seoul 151-744, Republic of Korea*

[5] *Institut für Quantenoptik und Quanteninformation, Österreichische Akademie der Wissenschaften, Technikerstraße 21a, 6020 Innsbruck, Austria*

(Received 17 July 2019; published 23 October 2019)

We present a numerical study of a microelectromechanical-system-based design of a fiber cavity integrated with an ion-trap system. Each fiber mirror is supported by a microactuator that controls the mirror's position in three dimensions. The mechanical stability is investigated by a feasibility analysis, which shows that the actuator offers stable support of the fiber. The actuators move the fibers' positions continuously with a stroke of more than 10 μm, with mechanical resonance frequencies on the order of kilohertz. A calculation of the trapping potential shows that a separation between the ion and the fiber consistent with strong ion-cavity coupling is feasible. Our miniaturized ion-photon interface constitutes a viable approach to integrated hardware for quantum information.

DOI: 10.1103/PhysRevApplied.12.044052

I. INTRODUCTION

The trapped-ion system is one of the most promising candidates for quantum-information processing [1,2]. Recent progress includes the generation of entanglement across 20 individually controlled ions [3], memory times exceeding 10 min [4], and a single-qubit gate fidelity of 99.9999% [5]. When these advantages are combined with those of optical cavities, the ion-cavity setting can be used to realize classical simulations [6–8] and is expected to enable efficient quantum networks [9,10]. Moreover, the cavity field mediates a long-range interaction between ions, which makes the system a suitable platform to study many-body physics such as structural phase transitions [11,12].

To demonstrate quantum advantage with ion-based quantum devices, that is, to solve classically intractable problems [13], it will be necessary to scale up traps to store and manipulate tens or hundreds of qubits. Coupling such ion traps to optical cavities, we can develop advanced quantum-information systems, such as a quantum repeater node comprising memory and communication qubit ions [1] and a modular quantum computer distributed across a photonic network [14,15]. To address the challenge of scalability, one solution is to use microelectromechanical system (MEMS) fabrication technology to miniaturize an ion-cavity system.

MEMS-based ion-trap technology is regarded as a promising platform to build large-scale quantum systems [16,17]. The first MEMS surface ion trap was fabricated at NIST Boulder in 2005 [18] by evaporation of Au electrodes on fused silica. A MEMS surface ion trap has a smaller trap depth than a three-dimensional Paul trap [19] but has the advantage of a reconfigurable planar trapping geometry, along with extensive optical access for laser beams, as required for a large-scale ion-trap quantum computer. In 2016, a MEMS trap called the "High Optical Access 2.0 trap" was developed by Sandia National Laboratories [20], and is widely used by many ion-trap researchers today. Topics of active research include the question of how to reduce stray charge accumulation (e.g., on the trap sidewalls [21] or via *in situ* cleaning [22,23]) and how to build increasingly sophisticated structures (e.g., junction traps [24,25]) for ion transport, and two- or three-dimensional electrode arrays [26,27].

MEMS-based ion traps have advantages in scalability and ease of fabrication, and they can also be easily integrated with other type of MEMS devices. MEMS

*tracy.northup@uibk.ac.at

†dicho@snu.ac.kr

‡These authors contributed equally to this work.

techniques can also reduce the footprint of the optical cavity system [28,29], particularly for the mirror actuators. The replacement of standard high-finesse mirrors by fiber mirrors has already reduced the physical cavity volume significantly [30,31]; however, when commercial nanopositioning stages are used, they place significant space demands on the in-vacuum assembly. Here we propose and investigate a design for a MEMS-based fiber-cavity system integrated with a surface ion trap. The fiber system is studied by our analyzing the mechanical stability, resonances, and stroke. Furthermore, we calculate the trapping potential seen by the ions so as to discuss the prospects for strong ion-cavity coupling.

II. BASIC CONCEPT

The main structure consists of a surface ion trap integrated with a MEMS-based fiber-cavity system [Fig. 1(a)]. The starting point is a microfabricated chip, detailed views of which are shown in Figs. 1(b) and 1(c), and which was previously described in Ref. [17]. The chip has a linear Paul-trap configuration in which two radio-frequency (rf) rails are used to generate a pseudopotential tube along the y axis. Axial confinement of ions is achieved by applying voltages to outer dc electrodes. The axis of the ion string is designed to align with that of the cavity such that multiple ions can be coupled to the cavity mode. Two inner dc rails define the principal axes of the trapping potential to ensure that the $\vec{k}$ vector of the Doppler cooling laser has overlap with all axes. The ion height above the trap surface may be controlled by adding rf voltages to the inner dc electrodes [32]. Between the two inner dc electrodes, a slot allows optical access to the ions from beneath the chip.

A cavity is formed by two fiber mirrors [30], each supported by a MEMS-based fiber stage, for which actuators offer three-dimensional position control, as shown in Figs. 1(a) and 1(d). A closer view of the stage is shown in Fig. 2(a). A V-shaped bench holding a fiber is fixed to each fiber stage, while the stage itself is suspended by thin beams, the other ends of which are connected to the surrounding actuators. Position control of the fiber stage is based on the mechanism of electrostatic actuation [28,33,34]: As described in detail in Sec. III, a comb-drive actuator provides continuous motion in the x-y plane. The fiber stage can be moved along the z axis via the electrostatic force between the stage and the fixed plate below. Such continuous positioning is intended to enable us to compensate for misalignment between the fiber mirrors, to align the cavity mode to the ion position, and to scan or lock the cavity frequency. The trapping chip and the fiber stages are fixed together with a common base plate with position-defining grooves. The fiber stages and trapping chip are glued individually to the base plate.

III. FIBER STAGE AND ACTUATOR

A. Mechanical stability

The mechanical stability of the fiber stage is investigated to check whether the stage can provide a safe support [35]. All numerical simulations for investigating mechanical properties are performed with COMSOL MULTIPHYSICS. We consider a fiber of SiO_2 with diameter of 250 μm glued on the fiber bench. The bench, the fiber stage, and the actuators are made of Si [36–39]. The load for the stage is conservatively estimated as 1.8 mg, including the fiber [40]. The mass and volume of the glue are ignored [41]. First, we numerically model the influence of the weight on the vertical stage position, with the results shown in Figs. 2(b) and 2(c). The load slightly shifts down the stage level due to gravity: the level of the stage descends by 0.97 μm for a beam width of 5 μm. The beams correspond to the dark-brown bridges indicated in Fig. 1(d). Each x-y actuator possesses 40 beams, so one fiber stage is controlled through 160 beams. For the calculations giving the results reported in Figs. 2(c) and 2(d), the width of all 160 beams is changed. Second, the factor of safety (FOS) is calculated. The FOS is defined as the yield stress divided by the working stress and has been commonly used to evaluate the mechanical stability of structures [42]. A system is considered to be a stable structure if the FOS is larger than 3. In our system, the FOS is minimized at the position of the largest curvature within the beams directly connected to the fiber stage [dotted gray circles in Fig. 2(b)]. In Fig. 2(d), we plot the minimum FOS as a function of the beam width. The FOS values obtained for several beam widths indicate that the stage is stable enough to support the fiber. Note that a fiber feedthrough is used to bring the fiber into the vacuum chamber in which the system is mounted. Tension between the fiber and the fiber feedthrough will exert an additional mechanical stress. This stress can be relieved by careful positioning of the fiber stage or by insertion of a strain-relieving stage (e.g., a piezoelectric element) between the fiber and the fiber feedthrough.

B. Positioning in three dimensions

We control the position of the stage in the x and y directions with comb-drive actuators using the electrostatic force [34,43,44]. Two- and three-dimensional comb-drive actuators have been demonstrated in various systems, such as microgrippers, atomic force microscopes, and scanning tunneling microscopes [45–48]. A single unit of the comb drive is shown in Fig. 3(a) to describe the working principle. The comb drive has two parts: a moving part and a stationary part. The capacitance between the two parts is given by

$$C(x) = \frac{2N\epsilon_0 h}{d}(x + x_0), \tag{1}$$

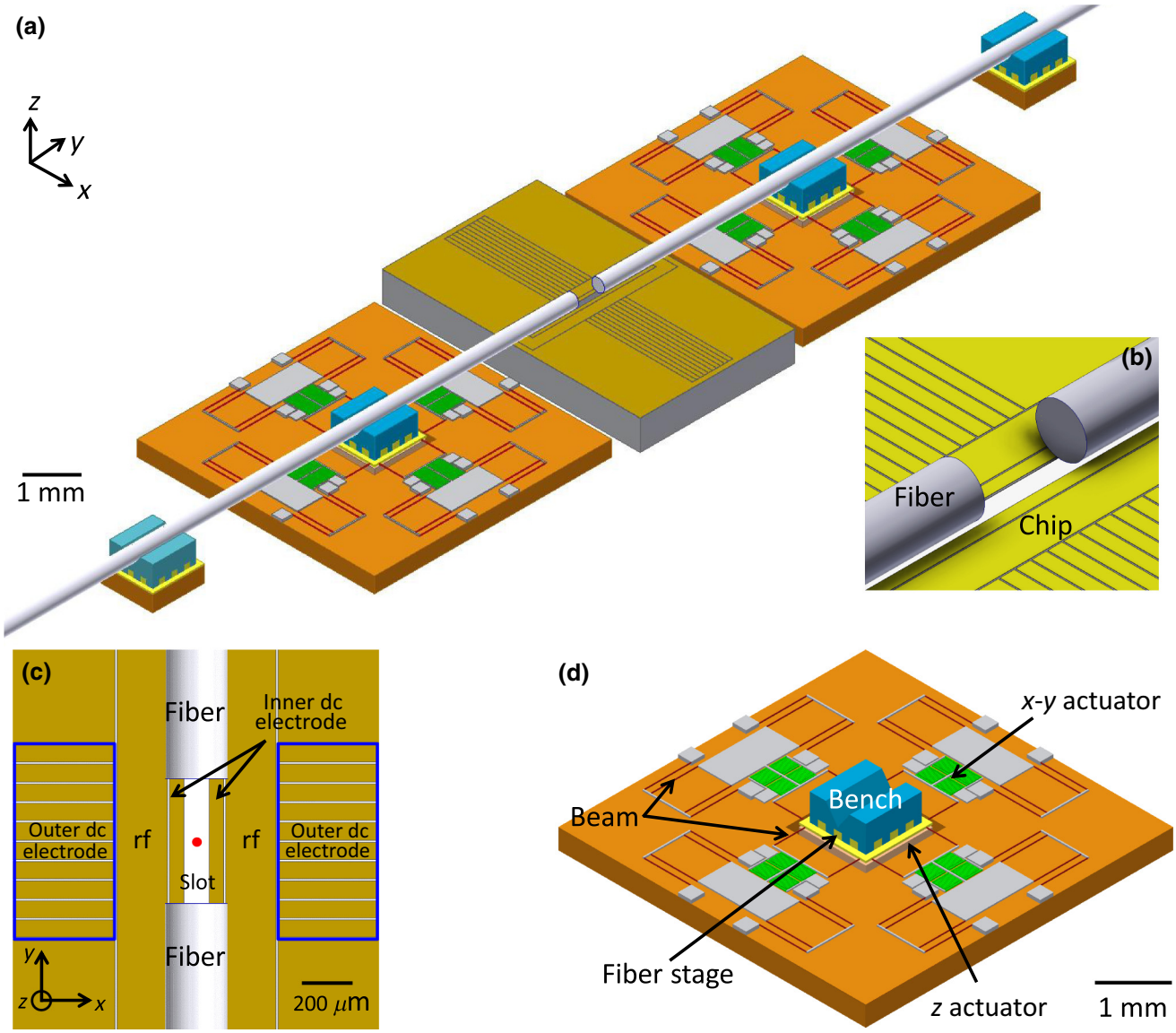

FIG. 1. (a) Overview of our design for a MEMS-based fiber cavity integrated with a surface ion trap. The central piece is the trapping chip, and the structures on both sides correspond to the fiber-cavity system. (b) Enlarged view of the ion-trapping site. (c) Electrode configuration of the chip, in which the rf rails, outer dc electrodes, and inner dc electrodes are indicated. Confinement along the cavity axis is achieved by voltages on the outer dc electrodes, marked by blue boxes. The red dot in the center indicates the ions' position. The gap between neighboring electrodes is 8 μm. (d) Detailed view of the fiber stage and actuators. A set of actuators control the position of the stage in three dimensions via beams. A fiber will be glued onto the V-shaped fiber bench.

where x is the displacement, x_0 is the overlapping length between the two parts along the displacement axis without a voltage difference, N is the total number of comb units, h is the thickness of the fingers, ϵ_0 is the dielectric constant of a vacuum, and d is the length of the gap between the two parts perpendicular to the displacement axis. If a voltage difference V is applied between the two parts, the exerted force can be expressed as

$$F = \frac{1}{2}\frac{\partial C}{\partial x}V^2 = \frac{N\epsilon_0 h}{d}V^2; \tag{2}$$

that is, the force is proportional to the change of the capacitance between two comb fingers. Here we assume that x_0 is large enough that side effects such as a fringe field can be ignored. This force results in a displacement of the moving part of

$$x = \frac{N\epsilon_0 h}{kd}V^2, \tag{3}$$

where k is the spring constant of the structure.

Our comb-drive configuration is shown in Figs. 3(b)–3(e). The comb drives indicated as "up" and "down"

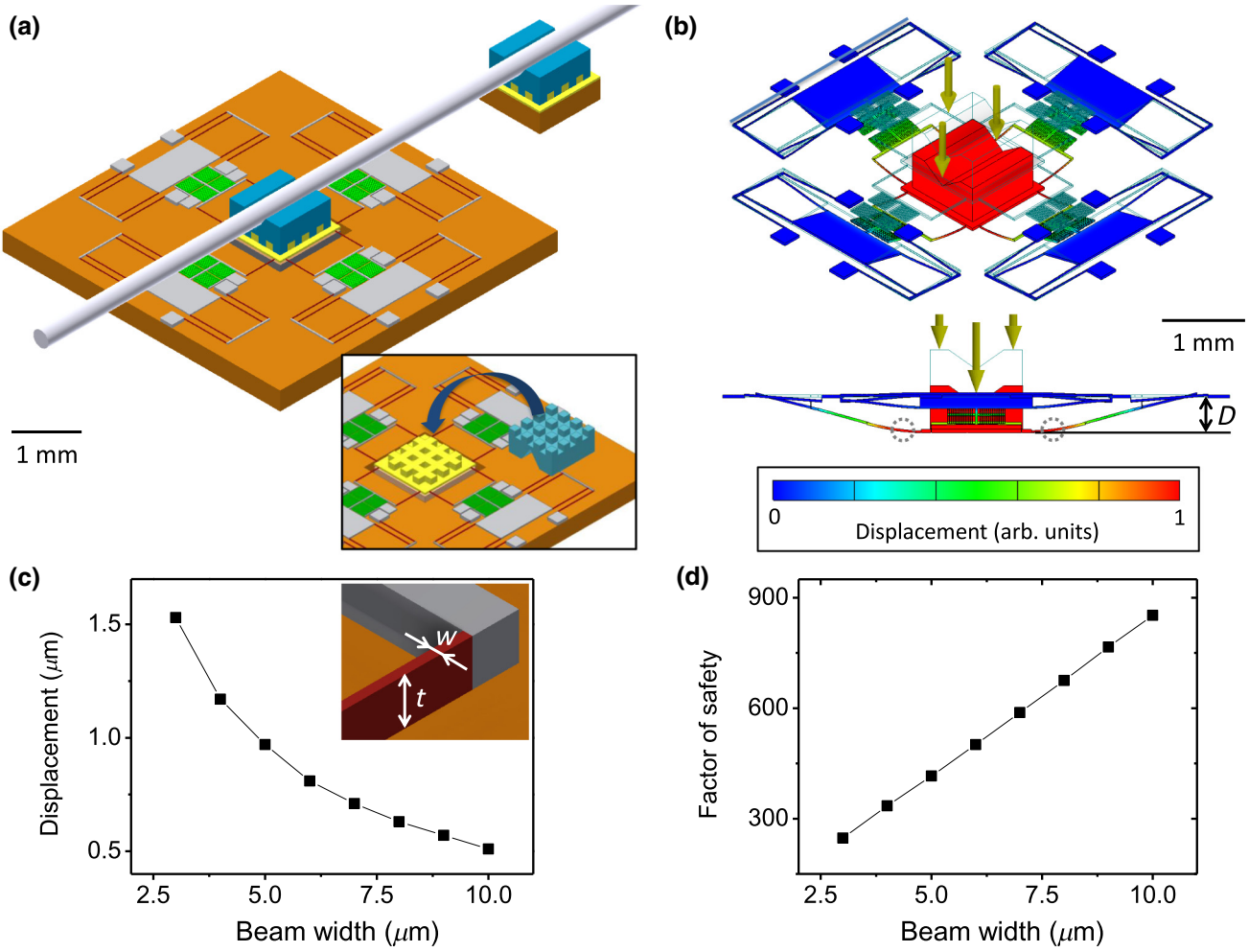

FIG. 2. Fiber stage and stability analysis. (a) The fiber stage with the fiber installed on the fiber bench. A second supporting stage can be used to relieve the load of the primary fiber stage. In the inset, plug-and-socket structures define the position of the bench with respect to the stage. (b) Equilibrium position of the stage, which is slightly shifted down due to gravity (fiber not shown). The dotted gray circles indicate the position of the minimum FOS in the whole structure. (c) Vertical displacement [D in (b)] as a function of beam width w, indicated in the inset. The beam thickness t, also indicated, is fixed at 20 μm for all simulations reported in this paper. (d) Factor of safety as a function of beam width.

in Fig. 3(b) induce motion along the x axis, and the drives indicated as "left" and "right" induce y-axis motion. Each comb drive has 120 teeth, such that in total the force of 240 teeth drives the motion along a given axis. As visualized in Fig. 3(b), if the position of a moving part is shifted, the force is transmitted between the comb drive and the fiber stage via beams on each side. The beams in the transverse directions are deflected by this motion. Figure 3(f) shows the simulation result of the stroke as a function of driving voltage for three different beam widths. As the width decreases, the beam becomes more elastic, which corresponds to a decreasing spring constant k. Hence, for a given voltage, the displacement is larger if the beam is thinner. As expected from Eq. (3), this displacement follows a quadratic scaling with respect to the driving voltage. One main benefit of MEMS actuators as compared with piezoelectric actuators is the larger stroke. In our case, for a beam width of 4 μm, we can cover one free spectral range of the fiber cavity (about 400 nm) with only 20 V. We also check the mechanical stability for the displacement along the x and y axes. As the displacement increases, the working stress to the actuator also increases, resulting in reduction of the FOS. Our calculated FOS values at a maximum applied voltage of 300 V correspond to 13, 21, 32, and 61 for beam widths of 4, 5, 6, and 8 μm, respectively, showing that our actuator is stable under the maximum displacement.

The position of the fiber stage along the z axis is controlled with the electrostatic force between the stage and another plate fixed below [see Figs. 4(a) and 4(b)]. This actuator for the z axis also uses a position-dependent capacitance. In Fig. 4(c), the simulation result shows the vertical displacement with respect to the driving voltage for three beam widths. It is notable that here too we obtain

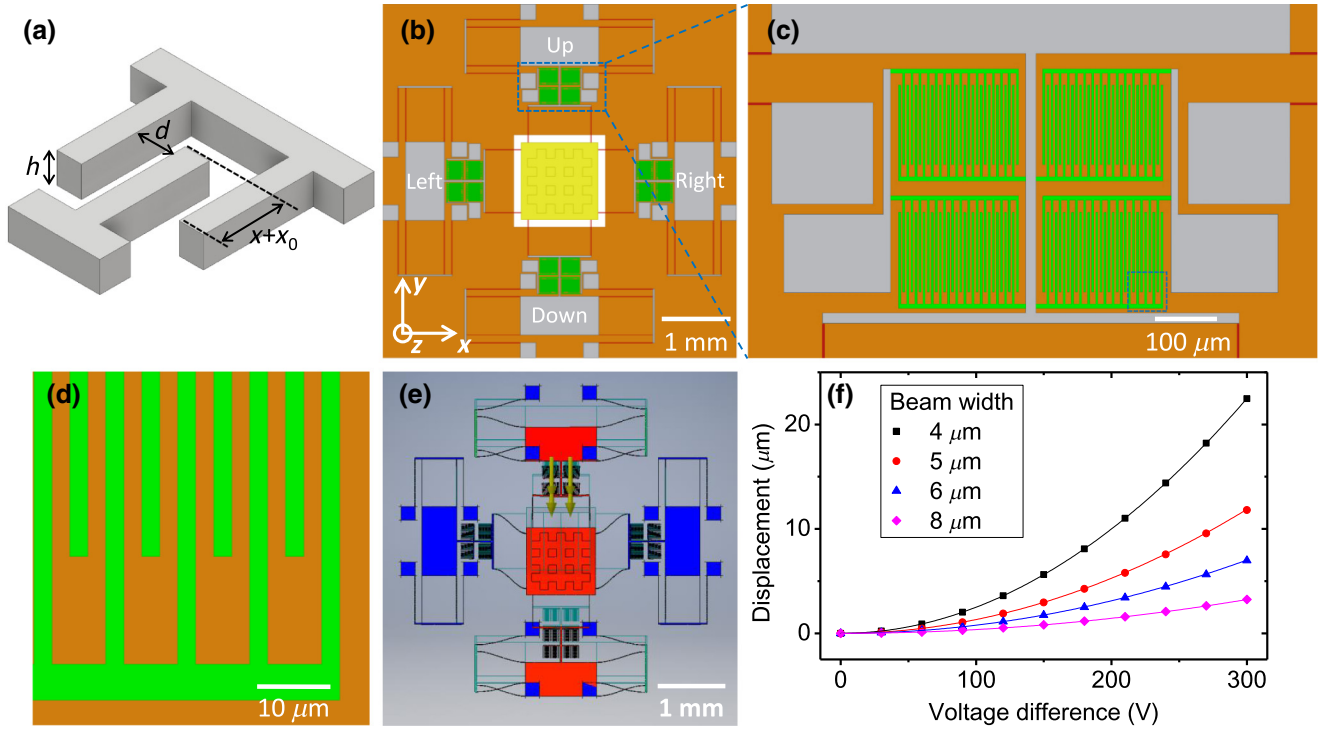

FIG. 3. (a) A single cell of the comb drive, with the thickness of the fingers h, the length of the gap between the two parts perpendicular to the displacement axis d, the displacement x, and the overlapping length between the two parts along the displacement axis without a voltage difference x_0. A voltage difference between the two parts changes their relative distance via the electrostatic force. (b) Top view of the fiber stage (center) with the plug-and-socket structure indicated. The stage is suspended from the comb drive via two beams on each side. The "left" and "right" comb drives move the stage along the x axis, and the comb drives denoted as "up" and "down" are used for the positioning along the y axis. (c) Enlarged view of the "up" comb structure. (d) Enlarged view of the blue box in (c). (e) Exaggerated displacement along the y axis. The beams in the direction orthogonal to the movement are deflected. (f) The stage displacement along the y axis is calculated as a function of the driving voltage for beam widths of 4 μm (black squares), 5 μm (red circles), 6 μm (blue triangles), and 8 μm (magenta diamonds). The solid lines are obtained by fitting with a quadratic function.

large strokes: for a beam width of 4 μm, the stage is displaced by 5 μm with an applied voltage of 160 V. The main difference from the comb drive is that when a voltage is applied, both the force and the distance between two plates change simultaneously: the distance d in Eq. (2) is also a function of V, resulting in a deviation from the V^2 scaling [Fig. 4(c)]. To check the mechanical stability, the FOS is calculated at the maximum applied voltage for each beam width. For beam widths of 4, 6, and 8 μm, we obtain FOS values of 81, 95, and 99 when voltage differences of 180, 210, and 240 V are applied for each width. These calculated results demonstrate the safety of the z-axis motion. More-complicated movements could be controlled by segmenting the electrodes on the lower plate. Separately applied voltages on these electrode segments would apply torque to the fiber stage, enabling rolling or pitching motion.

C. Mechanical resonances

The mechanical modes of the fiber stage and their resonance frequencies are calculated to estimate the mechanical bandwidth. For stabilization of the cavity frequency, it is desirable to achieve high mechanical bandwidth since it determines the maximum noise frequencies that can be suppressed [49]. This bandwidth is typically limited by the mechanical resonances of the actuator: phase shifts close to the resonance, accompanied by an amplitude response, would cause instabilities in the frequency stabilization [50]. Our simulation results are shown in Fig. 5 for a beam width of 8 μm. We find the lowest mechanical frequency of the stage as 985 Hz without the fiber [Fig. 5(a)] and investigate the six lowest mechanical resonances up to 7.27 kHz. With the fiber on top, the resonance frequency decreases due to the mass of the fiber with the lowest frequency of 633 Hz and the highest frequency of 4.87 kHz.

The mechanical resonance frequencies of our system are higher than those of commercially available stages but lower than those of recently reported fiber-cavity transducers [50–52]. If the resonances of our actuator are problematic for locking the cavity frequency in a future experiment, three methods can be used to improve the performance of the cavity lock. The first method consists in

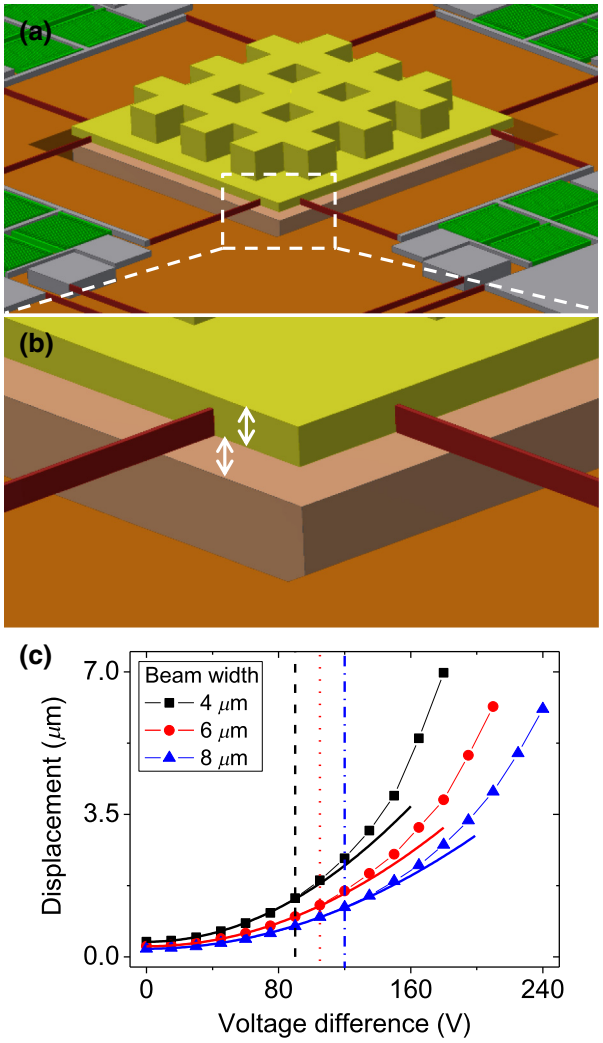

FIG. 4. The actuator for movement along the z axis. (a),(b) Views of the fiber stage (yellow) and the fixed plate underneath (gray). The thickness of the stage and the gap between the stage and the plate are both 30 μm [white arrows in (b)]. A voltage difference between the stage and the plate displaces the stage along the z axis via the electrostatic force. (c) Stage displacement along the z axis as a function of the voltage difference for a beam width of 4 μm (black squares), 6 μm (red circles), and 8 μm (blue triangles). The solid lines are fits to quadratic functions for comparison. The fitting range is from 0 V to the dashed black line for 4 μm, the dotted red line for 6 μm, and the dot-dashed blue line for 8 μm, for which V^2 scaling holds.

applying a feedback signal to the piezoelectric transducer of the optional secondary mount [Fig. 2(a)], which would extend the bandwidth to the standard level of the piezoactuators of several kilohertz. Another approach is to use the photothermal effect, using which a locking bandwidth of 400 kHz has been demonstrated in a fiber-cavity setting [51]. Finally, the phase lag in the vicinity of the resonance can be electronically compensated through digital filtering systems [53].

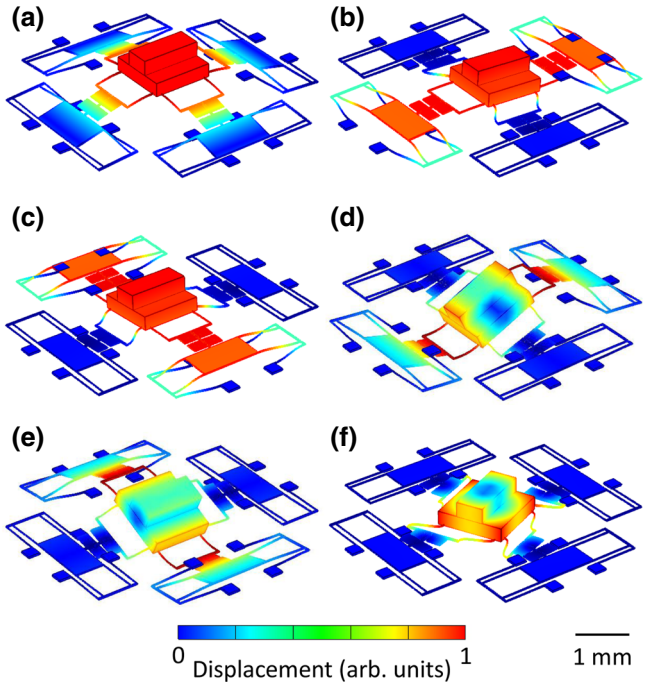

FIG. 5. Simulated mechanical modes of the fiber stage for a beam width of 8 μm, ordered by ascending frequency. The resonance frequencies without and with fibers are calculated as (a) 985 and 633 Hz, (b) 1.53 kHz and 952 Hz, (c) 1.62 kHz and 963 Hz, (d) 3.37 and 2.15 kHz, (e) 3.58 and 2.82 kHz, and (f) 7.27 and 4.87 kHz.

IV. TRAPPING POTENTIALS

Next we investigate the trapping potential for the ions. The total potential $\phi(r)_{\text{total}}$ is given by the sum of the pseudopotential generated by a rf voltage applied to the rf rails and the static potential $\phi(r)_{\text{dc}}$ derived from voltages on the outer dc electrodes and from charges on the fibers:

$$\phi(r)_{\text{total}} = \frac{q}{4m\Omega^2}|\vec{E}(r)|^2 + \phi(r)_{\text{dc}}, \tag{4}$$

where q and m represent the charge and mass of a single ion, respectively. The driving rf frequency Ω is chosen to be 20 MHz, and $\vec{E}(r)$ refers to the electric field due to the rf voltage. The calculation is done for $^{171}Yb^{+}$ ions with COMSOL MULTIPHYSICS. The rf amplitude is fixed at 150 V for all simulations of the trapping potentials, and dc voltages for each simulation are given in Ref. [40].

We characterize the trapping potential using two parameters: trap depth and trap frequency. The trap depth is defined as the potential difference between the minimum (at the trapping site) and the first local maximum of the profile along the x, y, and z axes. The trap frequency along each axis is obtained by our fitting the potential with a quadratic function. To exclude anharmonic regions of the potential profile, the fitting range is limited to ± 70 μm along the x axis, to ± 100 μm along the y axis, and between

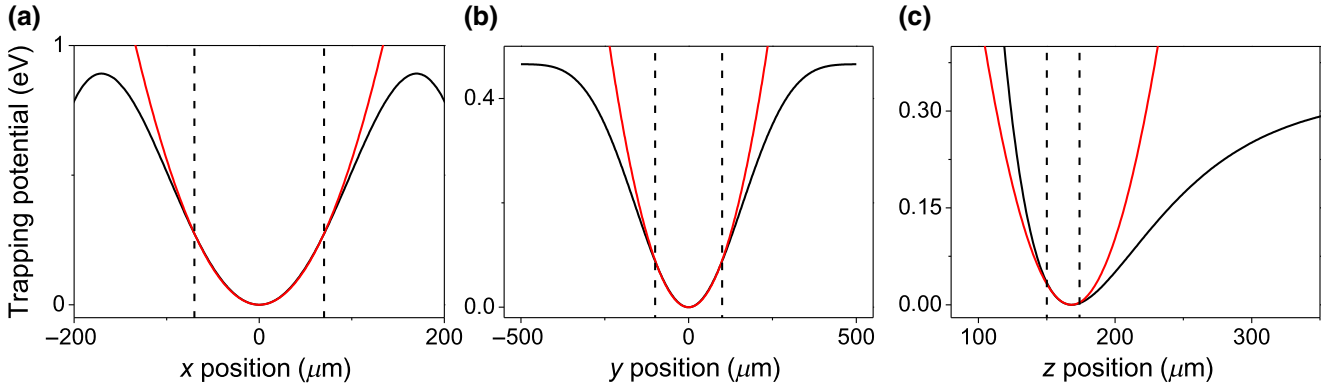

FIG. 6. Simulated trapping-potential profiles for a cavity of length of 1 mm comprising uncharged- and uncoated-fiber mirrors. The black lines are the results of calculations, and the red lines are obtained by fitting the data with quadratic functions. The fitting is done for the data between two vertical lines. The profile is shown along $(x, 0, 0)$ in (a), $(0, y, 0)$ in (b), and $(0, 0, z)$ in (c). The origin is the center of the trapping-chip surface.

-18 and $+6$ μm along the z axis. The trapping potential is calculated for three cases: (i) uncharged and uncoated fiber, (ii) uncharged fiber with metal coating on the sidewall, and (iii) charged fiber with metal coating.

A. Influence of fiber dielectrics

We begin with how the dielectric surface and volume of the fiber mirrors affect the trapping potential, assuming that the fibers are uncoated and have a neutral charge. In Fig. 6, trapping-potential profiles are presented along the x, y, and z axes for a cavity length of 1 mm. The trap frequencies obtained from fits to quadratic functions are $\omega_x/2\pi = 3.0$ MHz, $\omega_y/2\pi = 1.1$ MHz, and $\omega_z/2\pi = 2.4$ MHz [40]. The deviation of each profile with respect to that of a harmonic potential is below 5% for $|x| < 86$ μm, $|y| < 180$ μm, and -22 μm $< z < 5$ μm. The trap depth is 0.71, 0.46, and 0.33 eV in each direction. Figures 7(a) and 7(b) show the ion height above the trap and the trap frequency as a function of the cavity length. The trapping potentials are obtained in a step of 50 μm for a cavity length from 400 to 2000 μm. The height of the fibers' centers is fixed at 169 μm, overlapping with the height of the ion above the trap in the absence of the fibers. As the fibers are brought closer to the trapping site in our simulations, we find that the fibers have only a small influence on the potential for cavity lengths up to 500 μm. For this cavity length, we obtain trap frequencies of 3.0, 1.0, and 2.5 MHz and find that the ion height is unchanged. Therefore, if charges are absent from the fibers or can be removed by a discharging method [54], this bare fiber becomes an option to make a short cavity offering strong ion-cavity coupling (see Sec. V).

B. Influence of metal coating

We consider a situation in which the fibers' sidewalls are coated with a thin metal film, as has been used to provide an ultrahigh-vacuum-compatible coating in fiber-cavity experiments with neutral atoms and trapped ions [30,55–57]. This coating has two additional roles, along with protecting the fiber: the area of dielectric surface exposed to the ion is reduced, and a voltage can be applied to the fiber coating to compensate for distortion caused by charges on the dielectrics. In Figs. 7(c) and 7(d), the simulation result is shown for a grounded metal coating and uncharged-fiber facets. As the fibers are brought closer to the trap center, the height above the trap surface at which the potential minimum occurs decreases and the trap frequency increases. This behavior can be interpreted by considering grounded metal boundaries approaching the trapping site from far away in all directions. The potential energy becomes more confined as the metal structures come closer, leading to higher trap frequencies for shorter cavities. The effect is spatially symmetric along the x and y axes; however, the trapping chip makes it asymmetric along the z axis. In that case, one can consider a grounded metal boundary approaching from above and shifting down the position of the ion height.

The fiber height is fixed at 138 μm for all cavity lengths so that it coincides with the height of a trapped ion for a 500-μm-long cavity. This height is found in the following way: Fixing the cavity length at 500 μm, we calculate the trapping potential for fiber heights from 130 to 169 μm with a step of 1 μm so that we find the fiber height that corresponds to the ion height. Our calculation shows that the trapping potential for a 500-μm-long cavity has frequencies of 4.8, 1.3, and 4.1 MHz, and the shallowest trap depth is 0.29 eV in the $+z$ direction. The rf contribution to the potential along the y axis is negligible with bare fibers. In contrast, here the contribution of the rf psuedopotential is non-negligible along the y axis since the metal coating plays a role in determining the y-axis boundary conditions. This contribution would not affect micromotion compensation for a single

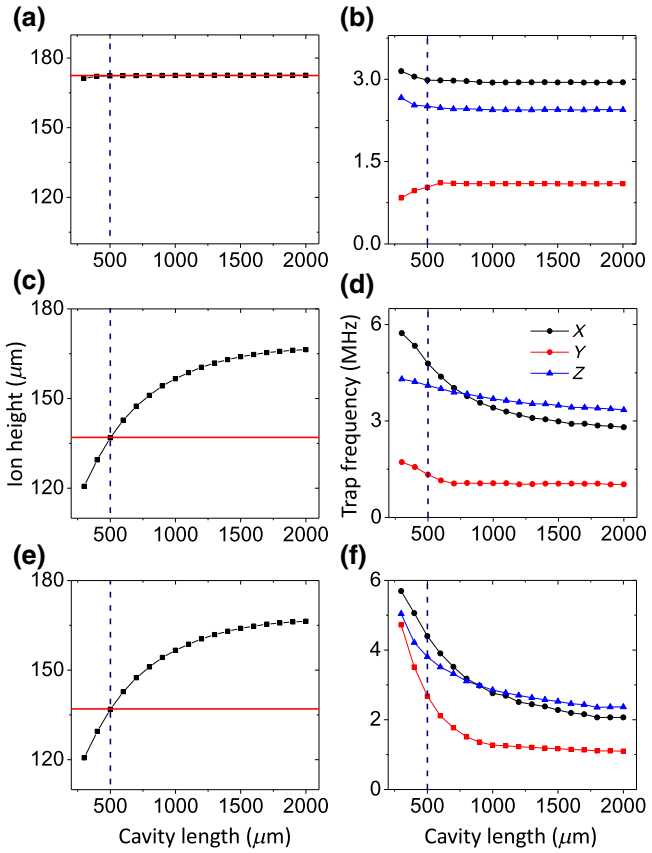

FIG. 7. Trapping-potential simulations for cavity lengths from 300 μm to 2.0 mm. Ion height above the trap surface and trap frequency are plotted as a function of the cavity length for uncharged and uncoated fibers in (a),(b), uncharged and metal-coated fibers in (c),(d), and charged and metal-coated fibers in (e),(f). The vertical navy lines indicate a cavity length of 500 μm, at which the strong-ion-cavity-coupling condition can hold (see Sec. V). In (a),(c),(e), the horizontal red line indicates the height of the fiber center, which is chosen to overlap with the height of an ion for a cavity length of 500 μm.

ion but would make compensation difficult for a long ion string.

C. Influence of charges

Next we investigate the influence of fiber charges on the trapping potential. As in Sec. IV B, we assume that the fiber sidewalls are metal coated. Here we make the additional assumption that both fiber facets are positively charged with a surface density of 5 $q/\mu\text{m}^2$. This assumption is based on a measurement in our ion-fiber cavity setting at the University of Innsbruck: causing a fiber to approach single ions for ion-fiber distances from 200 μm to 1.6 mm, we measure the ions' positions and trap frequencies, which are affected by the charges on the fibers, as a function of the ion-fiber distance. Reconstruction of the charge densities shows that the fibers are positively charged with densities on the order of several elementary charges in an area of 1 μm^2 [58]. In the current simulation, we choose a charge density of 5 $q/\mu\text{m}^2$, which is very close to a median of the reconstructed densities. The simulation result is shown in Figs. 7(e) and 7(f). The ion heights are similar to those found with an uncharged metal coating, and the fiber height is also fixed here at 138 μm. A notable feature is the rapid increase of the trap frequency along the y axis as the fibers are brought close to the trap center. This increase is because the positive charging makes the potential steeper along the y axis; negative surface charges would induce the opposite effect. The trapping potential for a 500-μm-long cavity is found to have frequencies of 4.4, 2.7, and 3.8 MHz. The shallowest trap depth is 0.13 eV along the $+z$ direction.

We would anticipate problems if the number of charges were slowly and randomly varying, as this would result in a time-dependent potential seen by the ion. We have previously observed timescales of such drifts to be from hours to days [58]. This problem could be solved either by use of a discharging method [54] or by application of compensation voltages to the metal coating. As long as the trap frequency can be monitored on timescales faster than those of the charge drifts, a feedback voltage can be applied to the metal coating to stabilize the trap frequency.

V. STRONG ION-CAVITY COUPLING

Strong atom-cavity coupling means that the atom-cavity coupling constant g (i.e., half of the rate of coherent energy exchange between the atom and the cavity field) is larger than both the atomic decay rate γ and the cavity-field decay rate κ [59]. The hallmark of strong atom-cavity coupling is the vacuum Rabi splitting, which originates from new atom-cavity eigenstates formed by the coupling [60]. This effect offers capabilities for exploring fundamental quantum optics [61] and implementing quantum-network protocols [62]. Furthermore, if strong coupling can be achieved, then by choosing a different cavity geometry, one also has access to the Purcell regime, in which $\kappa \gg g^2/\kappa \gg \gamma$ [62,63]. The Purcell regime enables efficient single-photon sources, a key ingredient for constructing a modular ion-based quantum-computer architecture [14,15,64].

To check whether strong ion-cavity coupling can be achieved with our design, we first plot calculated values of g and κ in Fig. 8(a), with γ given by the $^{174}\text{Yb}^+$ $|^2D_{3/2}\rangle$-$|^3D[3/2]_{1/2}\rangle$ transition at 935 nm. The radii of curvature of both fiber mirrors are fixed at 350 μm and the effective diameter (i.e., the diameter that is used to form a cavity mode) is fixed at 100 μm [65]. We assume a value of 97 000 for the cavity finesse, as reported in Ref. [65] for a recent fiber-cavity experiment. The finesse is a measure of the mirror losses and, together with the cavity length, allows κ to be determined. For a cavity length of 500 μm, the calculation results in $g/2\pi = 3.0$ MHz,

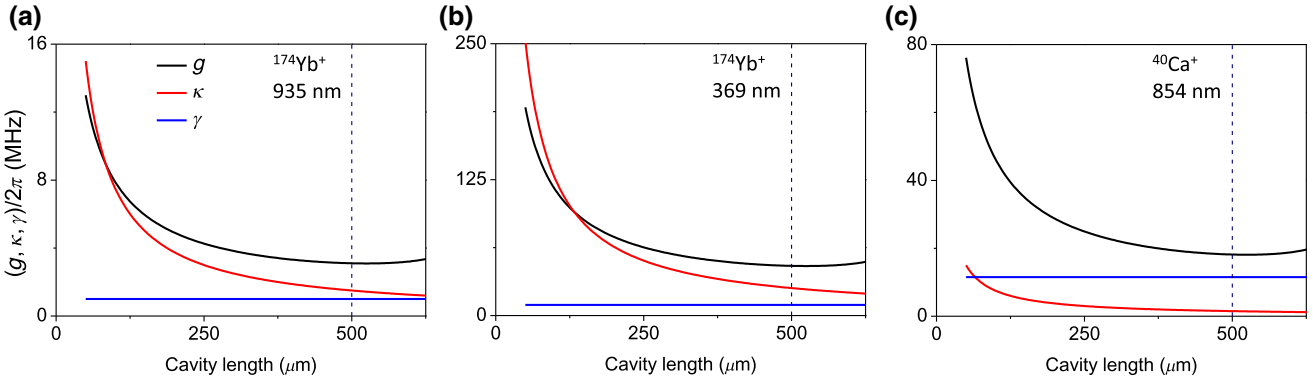

FIG. 8. Calculated values for g (black) and κ (red) plotted with the atomic linewidth γ (blue) for (a) the $^{174}\mathrm{Yb}^+$ $|^2D_{3/2}\rangle$-$|^3D[3/2]_{1/2}\rangle$ transition at 935 nm, (b) the $^{174}\mathrm{Yb}^+$ $|^2S_{1/2}\rangle$-$|^2P_{1/2}\rangle$ transition at 369 nm, and (c) the $^{40}\mathrm{Ca}^+$ $|^2D_{5/2}\rangle$-$|^2P_{3/2}\rangle$ transition at 854 nm. The vertical dashed lines indicate a cavity length of 500 μm, which is of particular relevance for our design (see the text for details).

$\kappa/2\pi = 1.0$ MHz, and $\gamma/2\pi = 1.5$ MHz, proving that the strong-coupling condition can be satisfied for the length on which we focused in the trapping-potential calculations.

In Fig. 8(b), we consider the $^{174}\mathrm{Yb}^+$ $|^2S_{1/2}\rangle$-$|^2P_{1/2}\rangle$ transition at 369 nm. The only different assumption here is a lower cavity finesse of 10 000, as reported in Ref. [66] and attributed to oxygen depletion in the mirror coating [66–68]. For a cavity length of 500 μm, we find that the strong-coupling condition still holds, with $g/2\pi = 46$ MHz, $\kappa/2\pi = 25$ MHz, and $\gamma/2\pi = 9.9$ MHz. While the 935-nm transition is more suitable for optical interconnects due to the lower absorption in optical fiber at this wavelength, the 369-nm transition enables significantly higher cavity coupling rates.

Finally, in Fig. 8(c), we investigate the $^{40}\mathrm{Ca}^+$ $|^2D_{5/2}\rangle - |^2P_{3/2}\rangle$ transition at 854 nm. Assuming the same finesse, radii of curvature, and effective diameter as in the calculation shown in Fig. 8(a), we obtain $g/2\pi = 18$ MHz, which is greater than both 1.5 MHz for $\kappa/2\pi$ and 11.5 MHz for $\gamma/2\pi$ at a cavity length of 500 μm. Taken together, the calculated results shown in Fig. 8 verify that our design can provide strong coupling for the transitions used in recent ion-fiber cavity experiments [31,56,66,68–70].

Although the simulations of our ion-trap design described in the previous sections are performed for $^{174}\mathrm{Yb}^+$ ions, it would be straightforward to adapt them for $^{40}\mathrm{Ca}^+$ ions.

VI. DISCUSSION

As presented thus far, our miniaturized ion-cavity setting exhibits safe fiber-mirror support with a large stroke, a stable ion-trapping potential, and feasible strong ion-cavity coupling. Moreover, our approach of combining a segmented ion trap with a cavity provides an additional advantage for optimizing alignment of the positions of multiple ions to the cavity field. Suppose that multiple ions are coupled to a cavity for a geometry in which the trap axis and the cavity axis are parallel to one another, as, for example, in Ref. [66]. Such a system would be useful for an efficient quantum-network node based on collective interactions [71]. One technical challenge in realizing this ion-cavity system consists of the incommensurability between the ion-ion distances and the spatial period of the cavity standing wave. While the ion-ion distances are determined by the harmonic potential and the repulsive Coulomb interaction between the ions, the cavity-field period corresponds to half of the resonant wavelength. Therefore, the strength of the coupling of each ion to the cavity field will be different, resulting in a reduced collective coupling rate as compared with the case in which each ion is coupled to an antinode of the cavity standing wave.

With our segmented trap design, through a particular choice of electrode voltages, it is possible to create a periodic trapping potential such that ions are equally spaced along the cavity axis so as to couple each ion with an individual antinode of the cavity standing wave [72]. The number of possible potential wells increases as more segmented electrodes are used. Alternatively, a boxlike quartic potential can be engineered by adjustment of the electrode voltages [73]. Here the ion-ion distance is predominantly determined by the repulsive Coulomb interaction, which aligns the ions equidistantly. In a recent demonstration, up to five ions were positioned near cavity-field antinodes on the basis of visibility measurements as a function of trap frequency [74]. This method, however, would be difficult to extend to control the positions of arbitrary numbers of ions.

To scale down the ion-cavity system even further, the surrounding elements of the setup can also be miniaturized [75], drawing on the technologies of microfabrication and MEMS to precisely integrate optical elements, photodetectors, and parts of the control electronics. There have been extensive experimental efforts to combine optical elements with surface traps at the micrometer scale or nanometer scale [76–78]. For example, optical fibers [79],

micromirrors, and a photodetector have been integrated to collect the ion fluorescence [80,81], MEMS mirrors have been used to address individual ions [82,83], and more-advanced optical elements, such as diffractive optics, have been integrated on a nanometer scale [84,85].

VII. CONCLUSION

We propose and investigate a design for MEMS-based manipulation of a fiber cavity integrated with a surface ion trap. The fiber stages are shown to be mechanically stable to support the fiber mirrors. The stages move continuously in three dimensions with strokes of up to tens of micrometers. The mechanical resonance frequencies of the stage and actuator are found to be on the order of kilohertz. Furthermore, we calculate a stable trapping potential generated for a 500-μm-long cavity, which should allow us to achieve strong ion-cavity coupling. This design for an on-chip ion-cavity system constitutes a promising approach for constructing a scalable quantum network.

ACKNOWLEDGMENTS

This work was financially supported by the Austrian Science Fund (FWF) through Projects No. F4019-N23, No. V252, and No. M1964, by the U.S. Army Research Laboratory's Center for Distributed Quantum Information via the project SciNet: Scalable Ion-Trap Quantum Network (Cooperative Agreement No. W911NF15-2-0060), by the Innsbruck-Seoul ION Trap Project, and by the Ministry of Science and ICT, Korea, under the Information Technology Research Center support program (Grant No. IITP-2019-2015-0-00385), supervised by the Institute for Information and Communications Technology Promotion.

[1] C. Monroe and J. Kim, Scaling the ion trap quantum processor, Science **339**, 1164 (2013).
[2] Philipp Schindler, Daniel Nigg, Thomas Monz, Julio T. Barreiro, Esteban Martinez, Shannon X. Wang, Stephan Quint, Matthias F. Brandl, Volckmar Nebendahl, Christian F. Roos, Michael Chwalla, Markus Hennrich, and Rainer Blatt, A quantum information processor with trapped ions, New J. Phys. **15**, 123012 (2013).
[3] Nicolai Friis, Oliver Marty, Christine Maier, Cornelius Hempel, Milan Holzäpfel, Petar Jurcevic, Martin B. Plenio, Marcus Huber, Christian Roos, Rainer Blatt, and Ben Lanyon, Observation of Entangled States of a Fully Controlled 20-Qubit System, Phys. Rev. X **8**, 021012 (2018).
[4] Ye Wang, Mark Um, Junhua Zhang, Shuoming An, Ming Lyu, Jing-Ning Zhang, L.-M. Duan, Dahyun Yum, and Kihwan Kim, Single-qubit quantum memory exceeding ten-minute coherence time, Nat. Photon. **11**, 646 (2017).
[5] T. P. Harty, D. T. C. Allcock, C. J. Ballance, L. Guidoni, H. A. Janacek, N. M. Linke, D. N. Stacey, and D. M. Lucas, High-fidelity Preparation, Gates, Memory, and Readout of a Trapped-ion Quantum bit, Phys. Rev. Lett. **113**, 220501 (2014).
[6] Alexei Bylinskii, Dorian Gangloff, and Vladan Vuletić, Tuning friction atom-by-atom in an ion-crystal simulator, Science **348**, 1115 (2015).
[7] Dorian Gangloff, Alexei Bylinskii, Ian Counts, Wonho Jhe, and Vladan Vuletić, Velocity tuning of friction with two trapped atoms, Nat. Phys. **11**, 915 (2015).
[8] Alexei Bylinskii, Dorian Gangloff, Ian Counts, and Vladan Vuletié, Observation of Aubry-type transition in finite atom chains via friction, Nat. Mater. **15**, 717 (2016).
[9] D. L. Moehring, P. Maunz, S. Olmschenk, K. C. Younge, D. N. Matsukevich, L.-M. Duan, and C. Monroe, Entanglement of single-atom quantum bits at a distance, Nature **449**, 68 (2007).
[10] T. E. Northup and R. Blatt, Quantum information transfer using photons, Nat. Photon. **8**, 356 (2014).
[11] T. Fogarty, C. Cormick, H. Landa, Vladimir M. Stojanović, E. Demler, and Giovanna Morigi, Nanofriction in Cavity Quantum Electrodynamics, Phys. Rev. Lett. **115**, 233602 (2015).
[12] Katharina Rojan, Rebecca Kraus, Thomás Fogarty, Hessam Habibian, Anna Minguzzi, and Giovanna Morigi, Localization transition in the presence of cavity backaction, Phys. Rev. A **94**, 013839 (2016).
[13] J. Preskill, Quantum computing and the entanglement frontier, arXiv:1203.5813 (2012).
[14] C. Monroe, R. Raussendorf, A. Ruthven, K. R. Brown, P. Maunz, L.-M. Duan, and J. Kim, Large-scale modular quantum-computer architecture with atomic memory and photonic interconnects, Phys. Rev. A **89**, 022317 (2014).
[15] Taehyun Kim, Peter Maunz, and Jungsang Kim, Efficient collection of single photons emitted from a trapped ion into a single-mode fiber for scalable quantum-information processing, Phys. Rev. A **84**, 063423 (2011).
[16] D. Kielpinski, C. Monroe, and D. J. Wineland, Architecture for a large-scale ion-trap quantum computer, Nature **417**, 709 (2002).
[17] Dong-Il Dan Cho, Seokjun Hong, Minjae Lee, and Taehyun Kim, A review of silicon microfabricated ion traps for quantum information processing, Micro. Nano. Syst. Lett. **3**, 2 (2015).
[18] J. Chiaverini, R. B. Blakestad, J. Britton, J. D. Jost, C. Langer, D. Leibfried, R. Ozeri, and D. J. Wineland, Surface-electrode architecture for ion-trap quantum information processing, Quantum Inf. Comput. **5**, 419 (2005).
[19] M. Brownnutt, G. Wilpers, P. Gill, R. C. Thompson, and A. G. Sinclair, Monolithic microfabricated ion trap chip design for scaleable quantum processors, New J. Phys. **8**, 232 (2006).
[20] Peter Maunz, Sandia National Laboratories Report No. SAND-2016-0796R 618951 (2016).
[21] S. Hong, Y. Kwon, C. Jung, M. Lee, T. Kim, and D. D. Cho, A new microfabrication method for ion-trap chips that reduces exposure of dielectric surfaces to trapped ions, J. Microelectromech. Syst. **27**, 28 (2018).
[22] D. A. Hite, Y. Colombe, A. C. Wilson, K. R. Brown, U. Warring, R. Jördens, J. D. Jost, K. S. McKay, D. P. Pappas, D. Leibfried, and D. J. Wineland, 100-fold Reduction of Electric-field Noise in an Ion Trap Cleaned with in

Situ Argon-ion-beam Bombardment, Phys. Rev. Lett. **109**, 103001 (2012).

[23] D. A. Hite, Y. Colombe, A. C. Wilson, D. T. C. Allcock, D. Leibfried, D. J. Wineland, and D. P. Pappas, Surface science for improved ion traps, MRS Bull. **38**, 826 (2013).

[24] J. M. Amini, H. Uys, J. H. Wesenberg, S. Seidelin, J. Britton, J. J. Bollinger, D. Leibfried, C. Ospelkaus, A. P. VanDevender, and D. J. Wineland, Toward scalable ion traps for quantum information processing, New J. Phys. **12**, 033031 (2010).

[25] D. L. Moehring, C. Highstrete, D. Stick, K. M. Fortier, R. Haltli, C. Tigges, and M. G. Blain, Design, fabrication and experimental demonstration of junction surface ion traps, New J. Phys. **13**, 075018 (2011).

[26] S. Seidelin, J. Chiaverini, R. Reichle, J. J. Bollinger, D. Leibfried, J. Britton, J. H. Wesenberg, R. B. Blakestad, R. J. Epstein, D. B. Hume, W. M. Itano, J. D. Jost, C. Langer, R. Ozeri, N. Shiga, and D. J. Wineland, Microfabricated Surface-electrode Ion Trap for Scalable Quantum Information Processing, Phys. Rev. Lett. **96**, 253003 (2006).

[27] Guido Wilpers, Patrick See, Patrick Gill, and Alastair G. Sinclair, A monolithic array of three-dimensional ion traps fabricated with conventional semiconductor technology, Nat. Nanotechnol. **7**, 572 (2012).

[28] C. O. Gollasch, Z. Moktadir, M. Kraft, M. Trupke, S. Eriksson, and E. A. Hinds, A three-dimensional electrostatic actuator with a locking mechanism for microcavities on atom chips, J. Micromech. Microeng. **15**, S39 (2005).

[29] P. Srinivasan, C. O. Gollasch, and M. Kraft, Three dimensional electrostatic actuators for tunable optical micro cavities, Sens. Actuators A-Phys. **161**, 191 (2010).

[30] D. Hunger, T. Steinmetz, Y. Colombe, C. Deutsch, T. W. Hänsch, and J. Reichel, A fiber Fabry–Perot cavity with high finesse, New J. Phys. **12**, 065038 (2010).

[31] Hiroki Takahashi, Ezra Kassa, Costas Christoforou, and Matthias Keller, Cavity-induced anticorrelated photon-emission rates of a single ion, Phys. Rev. A **96**, 023824 (2017).

[32] Ivan A. Boldin, Alexander Kraft, and Christof Wunderlich, Measuring Anomalous Heating in a Planar Ion Trap with Variable Ion-surface Separation, Phys. Rev. Lett. **120**, 023201 (2018).

[33] William C. Tang, Tu-Cuong H. Nguyen, and Roger T. Howe, Laterally driven polysilicon resonant microstructures, Sens. Actuators **20**, 25 (1989).

[34] Rob Legtenberg, A. W. Groeneveld, and M. Elwenspoek, Comb-drive actuators for large displacements, J. Micromech. Microeng. **6**, 320 (1996).

[35] W. C. Tang, M. G. Lim, and R. T. Howe, Electrostatic comb drive levitation and control method, J. Microelectromech. Syst. **1**, 170 (1992).

[36] B. Diem, P. Rey, S. Renard, S. Viollet Bosson, H. Bono, F. Michel, M. T. Delaye, and G. Delapierre, SOI 'SIMOX'; from bulk to surface micromachining, a new age for silicon sensors and actuators, Sens. Actuator A-Phys. **46**, 8 (1995).

[37] Renard Stéphane, Industrial MEMS on SOI, J. Micromech. Microeng. **10**, 245 (2000).

[38] J. Kim, S. Park, D. Kwak, H. Ko, W. Carr, J. Buss, and D. D. Cho, Robust SOI process without footing for ultra high-performance microgyroscopes, Sens. Actuator A-Phys. **114**, 236 (2004).

[39] Sangwoo Lee, Sangjun Park, and D. D. Cho, The surface/bulk micromachining (SBM) process: A new method for fabricating released MEMS in single crystal silicon, J. Microelectromech. Syst. **8**, 409 (1999).

[40] See Supplemental Material at http://link.aps.org/supplemental/10.1103/PhysRevApplied.12.044052 for our consideration of the mass of the fiber stage, the details of the simulation parameters, micromotion compensation of the ions, and a fabrication recipe for the fiber stage and the actuator.

[41] T. Goettsche, C. Ruddy, U. Heller, M. Stehr, H. Ashauer, T. Lindemann, P. Koltay, Y. Yu, R.-P. Peters, P. Soriani, and A. Bellone, Comparison of bonding procedures for 3D-structured polyimide films on silicon substrates applied to ink-jet cartridges, Int. J. Adv. Manuf. Technol. **33**, 191 (2007).

[42] F. P. Miller, A. F. Vandome, and M. B. John, *Factor of Safety* (VDM Publishing, Saarbrücken, 2010).

[43] Xinyu Liu, Keekyoung Kim, and Yu Sun, A MEMS stage for 3-axis nanopositioning, J. Micromech. and Microeng. **17**, 1796 (2007).

[44] M. Maroufi and S. O. R. Moheimani, A 2DOF SOI-MEMS nanopositioner with tilted flexure bulk piezoresistive displacement sensors, IEEE Sens. J. **16**, 1908 (2016).

[45] P.-F. Indermühle, V. P. Jaecklin, J. Brugger, C. Linder, N. F. de Rooij, and M. Binggeli, AFM imaging with an *xy*-micropositioner with integrated tip, Sens. Actuators A-Phys. **47**, 562 (1995).

[46] C. J. Kim, A. P. Pisano, and R. S. Muller, Silicon-processed overhanging microgripper, J. Microelectromech. Syst. **1**, 31 (1992).

[47] Y. Ando, Development of three-dimensional electrostatic stages for scanning probe microscope, Sens. Actuators A-Phys. **114**, 285 (2004).

[48] M. Maroufi, A. G. Fowler, and S. O. R. Moheimani, Mems for nanopositioning: Design and applications, J. Microelectromech. Syst. **26**, 469 (2017).

[49] Travis C. Briles, Dylan C. Yost, Arman Cingöz, Jun Ye, and Thomas R. Schibli, Simple piezoelectric-actuated mirror with 180 kHz servo bandwidth, Opt. Express **18**, 9739 (2010).

[50] J. Gallego, S. Ghosh, S. K. Alavi, W. Alt, M. Martinez-Dorantes, D. Meschede, and L. Ratschbacher, High-finesse fiber fabry-perot cavities: Stabilization and mode matching analysis, Appl. Phys. B **122**, 47 (2016).

[51] Johannes F. S. Brachmann, Hanno Kaupp, Theodor W. Hänsch, and David Hunger, Photothermal effects in ultra-precisely stabilized tunable microcavities, Opt. Express **24**, 21205 (2016).

[52] Erika Janitz, Maximilian Ruf, Yannik Fontana, Jack Sankey, and Lilian Childress, High mechanical bandwidth fiber-coupled Fabry–Perot cavity, Opt. Express **25**, 20932 (2017).

[53] Albert Ryou and Jonathan Simon, Active cancellation of acoustical resonances with an FPGA FIR filter, Rev. Sci. Instrum. **88**, 013101 (2018).

[54] S. E. Pollack, M. D. Turner, S. Schlamminger, C. A. Hagedorn, and J. H. Gundlach, Charge management for

gravitational-wave observatories using UV LEDs, Phys. Rev. D **81**, 021101 (2010).
[55] Yves Colombe, Tilo Steinmetz, Guilhem Dubois, Felix Linke, David Hunger, and Jakob Reichel, Strong atom-field coupling for Bose-Einstein condensates in an optical cavity on a chip, Nature **450**, 272 (2007).
[56] M. Steiner, H. M. Meyer, J. Reichel, and M. Köhl, Photon Emission and Absorption of a Single Ion Coupled to an Optical-fiber Cavity, Phys. Rev. Lett. **113**, 263003 (2014).
[57] Nina Podoliak, Hiroki Takahashi, Matthias Keller, and Peter Horak, Comparative Numerical Studies of Ion Traps with Integrated Optical Cavities, Phys. Rev. Appl. **6**, 044008 (2016).
[58] F. R. Ong, K. Schüppert, P. Jobez, M. Teller, B. Ames, D. A. Fioretto, K. Friebe, M. Lee, Y. Colombe, R. Blatt, and T. E. Northup, "Probing surface charge densities on optical fibres with a trapped ion," (to be published).
[59] H. J. Kimble, Strong interactions of single atoms and photons in cavity QED, Phys. Scr. **1998**, 127 (1998).
[60] S. Haroche and J. M. Raimond, *Exploring the Quantum: Atoms, Cavities and Photons* (Oxford University Press, New York, 2006).
[61] H. Mabuchi and A. C. Doherty, Cavity quantum electrodynamics: Coherence in context, Science **298**, 1372 (2002).
[62] Andreas Reiserer and Gerhard Rempe, Cavity-based quantum networks with single atoms and optical photons, Rev. Mod. Phys. **87**, 1379 (2015).
[63] C. K. Law and H. J. Kimble, Deterministic generation of a bit-stream of single-photon pulses, J. Mod. Opt. **44**, 2067 (1997).
[64] D. Hucul, I. V. Inlek, G. Vittorini, C. Crocker, S. Debnath, S. M. Clark, and C. Monroe, Modular entanglement of atomic qubits using photons and phonons, Nat. Phys. **11**, 37 (2014).
[65] Konstantin Ott, Sebastien Garcia, Ralf Kohlhaas, Klemens Schüppert, Peter Rosenbusch, Romain Long, and Jakob Reichel, Millimeter-long fiber Fabry-Perot cavities, Opt. Express **24**, 9839 (2016).
[66] Marko Cetina, Alexei Bylinskii, Leon Karpa, Dorian Gangloff, Kristin M. Beck, Yufei Ge, Matthias Scholz, Andrew T. Grier, Isaac Chuang, and Vladan Vuletić, One-dimensional array of ion chains coupled to an optical cavity, New J. Phys. **15**, 053001 (2013).
[67] Dorian Gangloff, Molu Shi, Tailin Wu, Alexei Bylinskii, Boris Braverman, Michael Gutierrez, Rosanna Nichols, Junru Li, Kai Aichholz, Marko Cetina, Leon Karpa, Branislav Jelenković, Isaac Chuang, and Vladan Vuletić, Preventing and reversing vacuum-induced optical losses in high-finesse tantalum (V) oxide mirror coatings, Opt. Express **23**, 18014 (2015).
[68] T. G. Ballance, H. M. Meyer, P. Kobel, K. Ott, J. Reichel, and M. Köhl, Cavity-induced backaction in purcell-enhanced photon emission of a single ion in an ultraviolet fiber cavity, Phys. Rev. A **95**, 033812 (2017).
[69] Matthias Steiner, Hendrik M. Meyer, Christian Deutsch, Jakob Reichel, and Michael Köhl, Single ion Coupled to an Optical Fiber Cavity, Phys. Rev. Lett. **110**, 043003 (2013).
[70] H. Takahashi, E. Kassa, C. Christoforou, and M. Keller, Strong coupling of a single ion to an optical cavity, arXiv:1808.04031 (2018).
[71] L. Lamata, D. R. Leibrandt, I. L. Chuang, J. I. Cirac, M. D. Lukin, V. Vuletić, and S. F. Yelin, Ion Crystal Transducer for Strong Coupling between Single Ions and Single Photons, Phys. Rev. Lett. **107**, 030501 (2011).
[72] J. P. Home and A. M. Steane, Electrode configurations for fast separation of trapped ions, Quantum Info. Comput. **6**, 289 (2006).
[73] G.-D. Lin, S.-L. Zhu, R. Islam, K. Kim, M.-S. Chang, S. Korenblit, C. Monroe, and L.-M. Duan, Large-scale quantum computation in an anharmonic linear ion trap, Europhys. Lett. **86**, 60004 (2009).
[74] Stephen Begley, Markus Vogt, Gurpreet Kaur Gulati, Hiroki Takahashi, and Matthias Keller, Optimized Multi-ion Cavity Coupling, Phys. Rev. Lett. **116**, 223001 (2016).
[75] Jungsang Kim and Changsoon Kim, Integrated optical approach to trapped ion quantum computation, Quantum Info. Comput. **9**, 181 (2009).
[76] J. True Merrill, Curtis Volin, David Landgren, Jason M. Amini, Kenneth Wright, S. Charles Doret, C.-S. Pai, Harley Hayden, Tyler Killian, Daniel Faircloth, Kenneth R. Brown, Alexa W. Harter, and Richart E. Slusher, Demonstration of integrated microscale optics in surface-electrode ion traps, New J. Phys. **13**, 103005 (2011).
[77] Peter F. Herskind, Shannon X. Wang, Molu Shi, Yufei Ge, Marko Cetina, and Isaac L. Chuang, Microfabricated surface ion trap on a high-finesse optical mirror, Opt. Lett. **36**, 3045 (2011).
[78] Andre Van Rynbach, George Schwartz, Robert F. Spivey, James Joseph, Geert Vrijsen, and Jungsang Kim, Design and characterization of an integrated surface ion trap and micromirror optical cavity, Appl. Opt. **56**, 6511 (2017).
[79] A. P. Van Devender, Y. Colombe, J. Amini, D. Leibfried, and D. J. Wineland, Efficient Fiber Optic Detection of Trapped ion Fluorescence, Phys. Rev. Lett. **105**, 023001 (2010).
[80] Amira M. Eltony, Shannon X. Wang, Gleb M. Akselrod, Peter F. Herskind, and Isaac L. Chuang, Transparent ion trap with integrated photodetector, Appl. Phys. Lett. **102**, 054106 (2013).
[81] Craig R. Clark, Chin-wen Chou, A. R. Ellis, Jeff Hunker, Shanalyn A. Kemme, Peter Maunz, Boyan Tabakov, Chris Tigges, and Daniel L. Stick, Characterization of Fluorescence Collection Optics Integrated with a Microfabricated Surface Electrode ion Trap, Phys. Rev. Appl. **1**, 024004 (2014).
[82] Caleb Knoernschild, Changsoon Kim, Felix Lu, and Jungsang Kim, Multiplexed broadband beam steering system utilizing high speed MEMS mirrors, Opt. Express **17**, 7233 (2009).
[83] S. Crain, E. Mount, S. Baek, and J. Kim, Individual addressing of trapped $^{171}Yb^{+}$ ion qubits using a microelectromechanical systems-based beam steering system, Appl. Phys. Lett. **105**, 181115 (2014).
[84] Amber L. Young, Jeff D. Hunker, A. R. Ellis, Sally Samora, Joel R. Wendt, Peter Maunz, and Daniel L. Stick, Precision alignment of integrated optics in hybrid microsystems, Appl. Opt. **53**, 6324 (2014).
[85] Karan K. Mehta, Colin D. Bruzewicz, Robert McConnell, Rajeev J. Ram, Jeremy M. Sage, and John Chiaverini, Integrated optical addressing of an ion qubit, Nat. Nanotechnol. **11**, 1066 (2016).